Environmental Fluid Mechanics
https://doi.org/10.1007/s10652-023-09948-8

ORIGINAL ARTICLE

Performance and flow dynamics of heavy air curtains using experiments and numerical simulations

Tanmay Agrawal[1] · Shresth Agarwal[1] · Vamsi Krishna Chalamalla[1] · Narsing Kumar Jha[1]

Received: 11 May 2023 / Accepted: 10 September 2023

Abstract

Air curtain devices (ACD) are commonly installed in domestic and commercial buildings to suppress the buoyancy-driven exchange flow through a doorway opening. Generally, the operating density of an ACD is equal to that of the indoor space making it neutrally buoyant. In the present study, we evaluate the performance of heavy air curtains where the operating density of the ACD is higher than that of the ambient fluid. The primary objective is to quantify the air curtain effectiveness, E, that determines the thermal comfort of building occupants based on the mean temperature inside the interrogated region. Experiments and numerical simulations are conducted and validated for various values of deflection modulus, D_m, that compare the relative magnitude of the jet momentum and transverse stack effect due to buoyancy. The other important non-dimensional parameter is the density ratio, S, which compares the extent of added buoyancy in ACD to that of across the doorway. In addition, the velocity dynamics of the air curtains are compared with an isothermal jet to understand the underlying effects that the buoyancy causes on the jet development. The general structure of air curtains that characterize the jet inclination and penetration is visualized through injecting a dye, and it agrees very well with the buoyancy distribution obtained using simulations at different D_m. Upon introduction of an assisting buoyancy, it has been found that the infiltration reduces by 25% compared to a neutrally buoyant air curtain for practical values of D_m.

Article Highlights

- Heavier air curtains are more effective as compared to the neutrally buoyant air curtains.
- The deceleration of mean centreline velocity is more prominent at smaller deflection modulus.
- Stability may be achieved at slightly smaller deflection modulus for heavier air curtains.

✉ Narsing Kumar Jha
narsingjha@am.iitd.ac.in

[1] Department of Applied Mechanics, Indian Institute of Technology Delhi, Hauz Khas, Delhi 110016, India

Keywords Building flows · Air curtains · Stratified flows · Sealing effectiveness

1 Introduction

Understanding the movement of air within and across a building provides useful insight into the distribution of various quantities such as temperature, pollutants, aerosols, dust, etc. This is also crucial for determining key metrics such as the thermal comfort and air quality index, which have been shown to affect human health, productivity, and general well-being [1, 2]. In most cases of building flows, this air movement is due to a temperature difference, the direction of which may be seasonal. In other cases, winds may cause the pressure-induced transport,varying with local topography and building design. Any unprotected opening in the fabric of such buildings, e.g., doorway, window, etc., therefore provides a passage for the heat losses and, may also cause an influx of dirt, pollutants, and insects, resulting in degradation of the conditioned indoor air quality of a building. Adopting a solid separator (wooden or metallic door, glass window, etc.) is the traditional approach towards suppressing such undesirable fluid exchange. While they are still a cost-effective solution, physical obstructions often create inconvenience in many commercial and domestic situations that involves significantly higher human or vehicular traffic. Therefore, technical advancements in building flow research have aimed to provide a non-obstructing barrier for traffic that is efficient to inhibit the movement of air, that may carry along with it the energy resulting in heat losses or dust and pollutants.

Air curtain devices (ACD) were originally conceived at the start of the 20th century. However, their adoption has increased significantly only over the last few decades. Fundamentally, ACD is a plane turbulent jet that blows across a doorway opening to suppress the buoyancy-induced movement of air [3]. They are usually driven by a centrifugal blower (in some cases, multiple blowers) and span along the entire width of the doorway. The dynamics of an air curtain flow closely resembles that of a plane turbulent impinging jet due to the presence of a wall (floor) [4]. Closer to the discharge nozzle, the velocity remains nearly constant in the potential core. A self-similar region persists a few jet widths downstream of the nozzle where the profile of the longitudinal velocity component exhibits a Gaussian variation in the lateral direction [5]. This self-similarity is affected closer to the wall, where the velocity decreases to zero. Under isothermal conditions, an air curtain is identical to a jet. As buoyancy is introduced across the two sides of the jet in the form of, for instance, a temperature difference, the resultant stack effect owing to this horizontal density stratification modifies the behavior of the planar jet. In particular, it provides a horizontal forcing that deflects the axis of the jet and could potentially deny its impingement.

The most common configuration of an ACD installation is that of a downward-blowing single air curtain unit as shown in Fig. 1; other configurations, including sideward-blowing, inclined, as well as an upward-blowing ACD, have also been considered in the past. In addition to these, the usage of a twin air curtain with an intermediate exhaust fan and a recirculating ACD has also been documented in the literature [6, 7]. Further possibilities in their variation arise from the operating conditions that include whether the primary air supply is drawn from inside or outside of a building and/or if any additional heating or cooling is done before discharging through the nozzle. An air curtain is said to be neutrally buoyant if its discharge density is the same as that of the density of the surrounding fluid it is being injected into. Whereas the density of a 'heavy' air curtain (HAC) is higher than the corresponding surrounding fluid. All these configurations have been developed over the years and are aimed

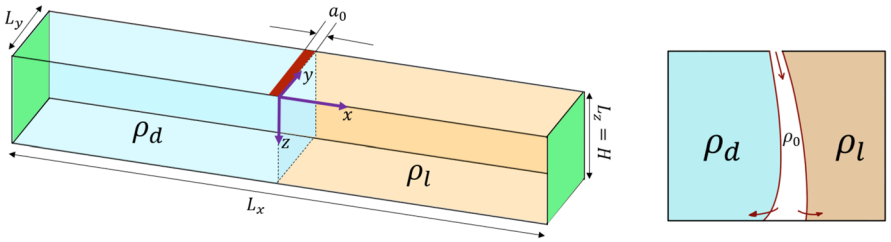

(a) Schematic of the problem (b) Cross-sectional view

Fig. 1 An overview of the air curtain installation. Blue and orange colors represent a colder and a warmer fluid respectively

at numerously distinct use cases. Some of them have been adopted extensively in cold room applications and refrigerated display cases to reduce the associated thermal losses [8–10], to suppress the contamination transport in building flows that include public buildings such as hospitals, industrial premises, and shopping complexes, etc. [11, 12]. Other applications include prevention of smoke spread in the case of a compartment or tunnel fire [13, 14], to improve the performance of a cooking range hood [15].

The experimental study conducted by Hayes and Stoecker [3] considered a vertically blowing air curtain and provided a systematic framework to evaluate the heat transfer characteristics of ACDs. They developed theoretical models, compared them with the experimental measurements, and found the agreement satisfactory. The characterization of the stability of ACDs was done using a dimensionless parameter, deflection modulus (D_m), which is mathematically defined as the ratio of the momentum flux contained within the ACD at nozzle exit and the transverse forces acting on it due to the stack effect as given below:

$$D_m = \frac{\rho_0 a_0 w_0^2}{gH^2(\rho_d - \rho_l)} \tag{1}$$

In this expression, ρ_0, ρ_l, and ρ_d denote the densities associated with the air curtain, lighter (warm), and dense (cold) fluids, respectively. The width of the ACD jet at the nozzle exit is represented as a_0 while the average discharge velocity is w_0. In Eq. (1), g is the acceleration due to gravity, and H is the height of the unprotected opening. Based on the conservation of momentum in the horizontal direction, they showed that a critical value of $D_{m,min} = \frac{1}{8}$ is needed to achieve an air curtain that could reach the other side of the doorway if we ignore the jet expansion owing to the entrainment of ambient fluid. If the deflection modulus is smaller than $D_{m,min}$, it is deflected sideways owing to the stack effect. The concept of deflection modulus has been proved to be robust over the years and is being actively used to characterize air curtain and study their behavior even today.

Another parameter that has been used to characterize the ACDs is sealing effectiveness, E. It compares the efficacy of air curtains in suppressing the buoyancy-induced fluid exchange as compared to the case when it is not installed, and the opening is considered unprotected. Mathematically, E is expressed as:

$$E = \frac{q - q_{ACD}}{q} = 1 - \frac{q_{ACD}}{q} \tag{2}$$

Here, q and q_{ACD} are volumetric exchange flow rates associated with a doorway opening in the absence and presence of an air curtain, respectively, and are quantified later in Sect. 3. An open door (OD) situation corresponds to an effectiveness of zero, whereas a perfectly sealed opening is obtained when $E = 1$. Past studies have shown that E depends on the deflection modulus, openings in the building fabric such as windows and exhausts, and the operating conditions e.g. jet angle, exit velocity, ambient temperature etc. [3, 8, 16–19]. D_m dependence of E has largely been documented for the neutrally buoyant air curtains (NBAC) where $\rho_0 = \rho_d$ for the configuration shown in Fig. 1a [8, 16, 17, 20, 21]. On the other hand, a heavy air curtain (HAC), which has an operating density larger than the ambient density is a relatively lesser studied problem. In the present study, we consider the case of a HAC installed on the cold (heavy) side with $\rho_0 > \rho_d$. The primary goal of this work is to compare the performance of a HAC installation with its neutral counterpart and the corresponding D_m dependence of effectiveness E. In the process, we provide quantitative differences in the velocity dynamics of an air curtain to that of an isothermal jet. In addition, we seek the implications of providing an assistive buoyancy in the indoor space. Specifically, we aim to understand how the infiltration of the ambient fluid of density ρ_l is neutralized by this assistive buoyancy (proportional to $\rho_0 - \rho_d$), when compared to a neutrally buoyant air curtain with $\rho_0 = \rho_d$.

The paper is organized as follows. The numerical framework of the employed Reynolds-averaged Navier–Stokes (RANS) and the large-eddy simulation (LES) methods is discussed in Sects. 2.1 and 2.2, respectively. Initial and boundary conditions for these simulations are also discussed therein in Sect. 2. All the experiments that were conducted are elaborated in Sect. 3 with a discussion on estimating the exchange flow rates. Section 4 presents an analytical model based on the conservation equations of mass, momentum, and buoyancy that can be used to estimate the properties associated with an air curtain at a steady state. In Sect. 5, the results from various simulations and experiments are discussed. The general flow field is illustrated in terms of buoyancy distribution in the domain as well as the velocity statistics along the centerline of the ACD jet. Subsequently, the estimates of the sealing effectiveness, E, are compared across different methodologies as a function of the deflection modulus. The implications of the positive buoyancy are discussed in Sect. 5.2.2. The major findings of the present work are summarized in Sect. 6.

2 Numerical simulations

The present study employs two methodologies to simulate the air curtain flows; Reynolds-averaged Navier–Stokes (RANS) and large-eddy simulation (LES). The overarching aim of the numerical simulations is to get the instantaneous fields of velocity and density which are not easily obtainable from experiments. The parameter space for all the different computations is tabulated in Table 1. A two-dimensional (2D) RANS solver is primarily employed to understand the parametric effect in ACD flows, and it is expected that their predictions may not be very accurate due to the various complexities associated with the problem, which will also be demonstrated later. Three-dimensional solvers, e.g., 3D RANS and LES, are used to obtain accurate quantitative estimates of the flow quantities involved. These simulations are conducted in a computational box of size $L_x = L = 2$ m, $L_y = W = 0.175$ m, $L_z = H = 0.35$ m. The size of this geometry is based on the *waterbath technique*, where the flow is established using water as the working fluid since the ratio of the kinematic viscosity of the two fluids, $\frac{\nu_{Air}}{\nu_{Water}}$, is approximately 15, therefore, such a simulation requires a smaller domain under similar

Table 1 Various computations that were conducted for different values of deflection modulus, D_m, and the buoyancy ratio, S, where $S = 0$ corresponds to the neutrally buoyant air curtain

$D_m \rightarrow$ 0.05 S		0.1	0.2	0.4	0.6	0.8	1.0	1.5
0	2D RANS	2D RANS	2D RANS	2D RANS	2D RANS	2D RANS	2D RANS	2D RANS
	3D RANS	3D RANS	3D RANS	3D RANS	–	3D RANS	–	–
	–	LES	LES	LES	–	LES	–	–
0.17	2D RANS	2D RANS	2D RANS	2D RANS	2D RANS	2D RANS	2D RANS	2D RANS
0.30	2D RANS	2D RANS	2D RANS	2D RANS	2D RANS	2D RANS	2D RANS	2D RANS
	3D RANS	3D RANS	–	3D RANS	–	3D RANS	–	–
	–	LES	LES	LES	–	LES	–	–
0.39	2D RANS	2D RANS	2D RANS	2D RANS	2D RANS	2D RANS	2D RANS	2D RANS

dynamic conditions [22]. Considering that the origin is taken at the center of the domain in the x-direction (see Fig. 1a), the region under investigation, i.e., the indoor space, spans from $x = -\frac{L}{2}$ to $x = 0$, whereas the ambient fluid is initially filled between $x = 0$ to $x = \frac{L}{2}$. The air curtain has a thickness of $a_0 = 5$ mm and is placed between $x = -a_0$ and $x = 0$ within the indoor space. Subsequently, the jet height to width ratio, $\frac{H}{a_0}$, is set to 70, which is required for ACD applications [17]. Various aspects of the computational setup are shown in Fig. 1, which also presents a cross-sectional view of the typical climatic separation in the presence of an air curtain. In these simulations, the ACD was modeled as a top-hat *velocity-inlet* boundary with a prescribed uniform velocity and turbulence intensity (see the red patch in Fig. 1a). The side faces at $x = \pm\frac{L}{2}$, shown as green, were enforced with a zero Neumann boundary condition to represent an *outflow* boundary. This configuration is generally chosen for the simulations of planar jets and accounts for possible lateral flow exits from both the indoor and outdoor spaces [23, 24]. A no-slip, no-penetration boundary condition is imposed on all the other walls in the domain. The mesh is refined in the central region where the air curtain operates to capture the large gradients in the flow associated with the development of flow instabilities and sharp-density interfaces.

Initially at $t = 0$, ρ_l and ρ_d are chosen such that it corresponds to $T_l = 45$ °C and $T_d = 25$ °C. The resulting reduced gravity due to this buoyancy difference, $g' = g\frac{\Delta\rho}{\rho_d}$, before the air curtain operates, is approximately 6.8 cm/s^2. These temperature levels are good representative values of a typical tropical region in the summer season. Herein, the primary objective of the air curtain installation is to ensure the thermal comfort of building occupants where the indoor temperature could change due to the infiltration of the outdoor warmer fluid. Therefore, the ACD should eliminate the undesirable fluid exchange between the two spaces in order to help prevent any temperature drops in indoors. Furthermore, for the air curtain to assist towards thermal comfort, an assistive buoyancy ($\rho_0 > \rho_d$) could potentially help in neutralizing any temperature increment due to fluid infiltration. The strength of this added buoyancy is quantified in the form of a dimensionless parameter, S, that compares the assistive buoyancy in the air curtain to the buoyancy difference across the doorway and can be mathematically written as:

$$S = \frac{\rho_0 - \rho_d}{\rho_d - \rho_l} \tag{3}$$

The present work reports simulations conducted for the jet temperature, T_j, ranging between 10 °C and 25 °C where $T_j = 25$ °C corresponds to a neutrally buoyant air curtain

(NBAC). Therefore, in the non-dimensional sense, S varies between 0 for an NBAC installation to approximately 0.39 for an air curtain with T_j= 10 °C. The inlet velocity, w_0, is changed to obtain different values of deflection modulus (D_m). The Reynolds number, Re, based on the air curtain parameters $\left(Re = \frac{w_0 a_0}{\nu}\right)$ is kept in a similar order (see Table 2) as that in full-scale installations to ensure dynamic similarity. For the heavy air curtains, the corresponding Richardson number, $Ri = \sqrt{\frac{g' a_0}{w_0^2}}$ is also tabulated that compares the relative magnitude of the added buoyancy (in the form of a reduced gravity) to that of the supplied momentum. It should be noted that Ri is related to the deflection modulus as $Ri = \left(\frac{a_0}{H}\right)\frac{1}{\sqrt{D_m}}$ and the chosen parameter space for Richardson number closely resemble a full-scale air curtain installation.

In the following subsections, a brief description of the simulation methodologies is presented. The reader may refer to the literature for the complete mathematical framework [25–27].

2.1 Reynolds-averaged Navier–Stokes (RANS)

RANS computations are based on the idea of Reynolds decomposition wherein any instantaneous flow parameter, for instance, a velocity component u_i, is partitioned into a mean (U_i) and fluctuating (u_i') part. The following set of equations is solved, which model the behavior of mean velocity and temperature fields under Boussinesq approximation as:

$$\frac{\partial U_i}{\partial x_i} = 0 \tag{4}$$

$$\frac{\partial U_i}{\partial t} + U_j\frac{\partial U_i}{\partial x_j} = -\frac{1}{\rho_0}\frac{\partial P}{\partial x_i} + \frac{\partial}{\partial x_j}\left[\nu\frac{\partial U_i}{\partial x_j} - \overline{u_i' u_j'}\right] - g[1-\beta(T-T_0)]\delta_{13} \tag{5}$$

$$\frac{\partial T}{\partial t} + U_j\frac{\partial T}{\partial x_j} = \frac{\partial}{\partial x_j}\left[\kappa\frac{\partial T}{\partial x_j} - \overline{u_j' T'}\right], \tag{6}$$

Table 2 The values of dimensionless parameters, Reynolds number (Re) and Richardson number (Ri), corresponding to heavy air curtains at various deflection modulus, D_m

w_0	D_m	$Re = \frac{w_0 a_0}{\nu}$	$Ri = \sqrt{\frac{g' a_0}{w_0^2}}$
0.286	0.05	1435	0.023
0.405	0.1	2025	0.016
0.573	0.2	2865	0.011
0.811	0.4	4050	0.008
0.997	0.6	4965	0.006
1.147	0.8	5730	0.005
1.571	1.5	7850	0.004

Here, $g' = g\left(\frac{\rho_0 - \rho_d}{\rho_0}\right)$, and therefore, $Ri_{NBAC} = 0$

Eqs. (4, 5, and 6) are the mathematical analog of the conservation laws of mass, momentum, and energy. P represents the mean fluid pressure and ρ_0 is the reference density. g is the acceleration due to gravity, and the fluid viscosity, thermal expansion coefficient, and thermal diffusivity are denoted by ν, β, and κ, respectively. The inclusion of Reynolds stresses $\overline{u_i' u_j'}$ and $\overline{u_j' T'}$ is an unavoidable consequence of Reynolds decomposition and poses a challenge to mathematical closure of this system of equations. In the present study, we employ the renormalization group (RNG) k-ϵ model [28] to close this system by solving additional equations for the turbulent kinetic energy, k, and the turbulent dissipation rate, ϵ. These are respectively given as:

$$\frac{Dk}{Dt} = \frac{\partial}{\partial x_i}\left[\left(\nu + \frac{\nu_t}{\sigma_k}\right)\frac{\partial k}{\partial x_i}\right] + \mathcal{P}_k + \mathcal{B}_k - \epsilon \tag{7}$$

$$\frac{D\epsilon}{Dt} = \frac{\partial}{\partial x_i}\left[\left(\nu + \frac{\nu_t}{\sigma_k}\right)\frac{\partial \epsilon}{\partial x_i}\right] + \frac{\epsilon}{k}\left(C_{1\epsilon}\mathcal{P}_k + C_{1\epsilon}(1 - C_{3\epsilon})\mathcal{B}_k - C^*_{2\epsilon}\epsilon\right) \tag{8}$$

In these equations, the operator $\frac{D}{Dt}$ symbolizes a material derivative that includes the effect of fluid advection. P_k represents the rate of production of turbulent kinetic energy due to mean flow and is evaluated as:

$$P_k = \nu_t\left[\frac{\partial U_i}{\partial x_j} + \frac{\partial U_j}{\partial x_i}\right]\frac{\partial U_i}{\partial x_j} \tag{9}$$

The turbulent viscosity, ν_t, in this expression is calculated as $\nu_t = C_\mu \frac{k^2}{\epsilon}$ where C_μ is a model coefficient. The production of turbulence due to buoyancy, $\mathcal{B}_k$, is an added term in Eqs. (7 and 8) to account for the effect of stratification and is given as:

$$\mathcal{B}_k = \beta g \rho_0 \frac{\nu_t}{\sigma_t}\frac{\partial T}{\partial z} \tag{10}$$

where σ_t is the turbulent Prandtl number. The constant $C^*_{2\epsilon}$ in Eq. (8) is given as:

$$C^*_{2\epsilon} = C_{2\epsilon} + \frac{C_\mu \eta^3 (1 - \eta/\eta_0)}{1 + \beta\eta^3} \tag{11}$$

Here, the parameter η is estimated as Sk/ϵ where $S = \sqrt{2S_{ij}S_{ij}}$ and $S_{ij} = \frac{1}{2}\left(\frac{\partial U_i}{\partial x_j} + \frac{\partial U_j}{\partial x_i}\right)$ is the strain rate. The values of coefficients associated with any turbulence model are generally based on empirical and experimental data. For the present work employing the RNG $k - \epsilon$ model, we have taken these as:

$$\begin{Bmatrix} C_\mu \\ C_{1\epsilon} \\ C_{2\epsilon} \\ \sigma_k \\ \eta_0 \\ \beta \end{Bmatrix} = \begin{Bmatrix} 0.0845 \\ 1.42 \\ 1.68 \\ 0.7194 \\ 4.38 \\ 0.012 \end{Bmatrix}$$

The ANSYS Fluent code, which is based on the finite-volume method (FVM), is utilized to solve these equations on two-dimensional and three-dimensional grids. Suitable meshes were chosen after a systematic mesh sensitivity study which is reported in Agrawal et al. [29]. The grids for the 2D and 3D RANS computations have 64,000 and 422,400 points, respectively. For both cases, at least ten cells span across the air curtain width, and the vertical (z) resolution is kept uniform at $\frac{a_0}{2}$. The spatial derivatives in the governing equations are approximated using a second-order upwind scheme. A second-order implicit method is employed to evaluate the temporal derivative, and the pressure and velocity fields are coupled using the Coupled algorithm. The methodology was validated for the case of a planar jet, and the results are presented in appendix 1.

2.2 Large-eddy simulation (LES)

The RANS approach involves modeling all the scales in a turbulent flow. On the other hand, an LES based-solver calculates the large scales explicitly, which generally play a crucial role in mass and momentum transfer, and models only the impact of small-scale eddies. This is achieved by using a spatial filtering operation to separate the large (resolved) scales from the small (subgrid) ones. The LES solver employed in the present study works on the following set of filtered continuity, momentum, and scalar equations using the Boussinesq approximation, and further assuming a linear relationship between density and the equation of state:

$$\frac{\partial \overline{u_i}}{\partial x_i} = 0 \tag{12}$$

$$\frac{\partial \overline{u_i}}{\partial t} + \overline{u_j}\frac{\partial \overline{u_i}}{\partial x_j} = -\frac{1}{\rho_0}\frac{\partial \overline{p}}{\partial x_i} - \overline{b}\,\delta_{i3} + \frac{\partial}{\partial x_j}\left[\nu\frac{\partial \overline{u_i}}{\partial x_j} - \tau_{ij}^R\right] \tag{13}$$

$$\frac{\partial \overline{b}}{\partial t} + \overline{u_j}\frac{\partial \overline{b}}{\partial x_j} = \kappa_b\frac{\partial}{\partial x_j}\left[\frac{\partial \overline{b}}{\partial x_j} - \lambda_{ij}^R\right] \tag{14}$$

where the i^{th} component of the filtered velocity field is denoted using $\overline{u_i}$, κ_b is the scalar diffusivity, $\overline{p}$ and $\overline{b} = g\overline{\rho}/\rho_0$ correspond to the filtered pressure and buoyancy fields respectively. An eddy-viscosity-based approximation models the anisotropic part of the subgrid stress tensor, $\tau_{ij}^R = \rho\overline{u_i u_j} - \rho\overline{u}_i\overline{u}_j$, and subgrid buoyancy flux, λ^R, as:

$$\tau_{ij}^R - \frac{1}{3}\tau_{kk}^R\delta_{ij} = -2\nu_{sgs}\overline{S}_{ij} \tag{15}$$

$$\lambda^R = -2\kappa_{sgs}\frac{\partial \overline{b}}{\partial x_j} \tag{16}$$

where $\overline{S}_{ij}$ represents the strain rate associated with the filtered velocity field. The subgrid-scale Prandtl number $Pr_{sgs} = \nu_{sgs}/\kappa_{sgs}$ has been taken as unity for all the reported LES simulations. The above set of equations is solved using the in-house code Stratified Ocean Model with Adaptive Refinement (SOMAR). Various kinds of stratified flows, including tidal flows, low mode wave scattering, gravity currents, internal and solitary waves

propagation, etc., have been studied in the past using SOMAR [30–34]. The numerical discretization in this solver is based on second-order finite differences for the advection, viscous and diffusion terms, whereas time advancement is done using the RK3 scheme. The grid employed in the present LES simulations comprises a base level containing $N_x \times N_y \times N_z = 1536 \times 32 \times 128$ points with a finer level overlaid in the central region having a refinement factor of 4, 2 and 4 in the x, y and z directions respectively. The spatial extent of the finer level is kept between $x = -0.05$ m to $x = 0.05$ m to accurately resolve the shear layers in the planar air curtain jet.

3 Experiments

The experiments are conducted in a glass tank of dimensions 2 m × 0.185 m × 0.4 m, a schematic of which is shown in Fig. 2. While an initial temperature difference is used in the simulations to create the desired buoyancy effect across the doorway, we dissolve table salt in freshwater to manipulate the fluid density in the experimental system. Using dissolved substances such as salt eliminates the need to create a thermally insulated system and, thus, greatly aids the ease with which the stratified flow measurements may be conducted and the flow may be visualized. The effect of different scalar diffusivity ($\kappa_T \approx 0.14$ mm^2/s, $\kappa_S \approx 0.0013$ mm^2/s) has shown to produce similar transport phenomenon associated with the macroscopic scales in buoyancy-driven flows [35–37]. While this may not be always true for full-scale measurements, this simplification is valid for similitude experiments such as those conducted in the present study [38]. Therefore, heat (temperature) and salt can be interchangeably used as stratifying agents when the macroscopic motions are concerned in a laboratory waterbath.

The tank was then divided into two equal sections using a perspex sheet (lock gate, denoted as LG) that spanned across the entire width of the facility and, thus, represented a doorway. The two halves were simultaneously filled using freshwater and saltwater, maintained at a density of ρ_l and ρ_d, respectively. Any minor fluid leakage across the lock gate due to hydrostatic pressure difference was carefully monitored during the filling process. In a separate test, this leakage was estimated to be within 5 ml/min, which corresponds to less than 0.5% of the total fluid volume at either side of the lock gate. The water level at the beginning of an experiment was kept at $H = 0.22$ m. Generally, the fluid level on the saltwater side was kept approximately 5 mm lower than the freshwater side to allow the establishment of ACD, which is described now.

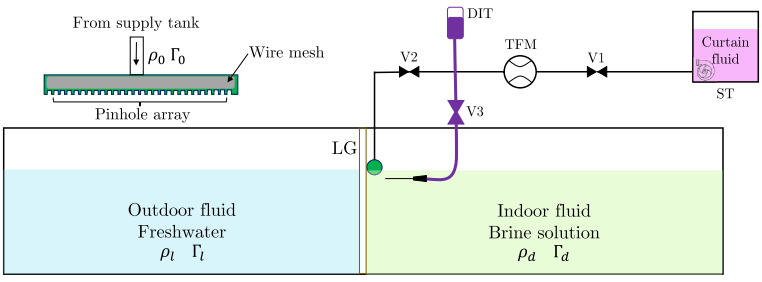

Fig. 2 Schematic of the experimental setup at the instant before removing the lock-gate. The curtain fluid is brine solution for the NBAC and aqueous solution of sugar for HAC

Table 3 Various experiments conducted in the present study

$D_m, \rho \rightarrow$ / S	ρ_0	ρ_d	ρ_l	D_m	δD_m
0	1035−1050	1035−1050	1000	0.05−0.1	$\mathcal{O}(0.01)$
	1022−1030	1022−1030	1000	0.12−0.16	$\mathcal{O}(0.02)$
	1014−1019	1014–1019	1000	0.19–0.25	$\mathcal{O}(0.04)$
	1009–1012	1009−1012	1000	0.30−0.40	$\mathcal{O}(0.05)$
	1004−1007	1004–1007	1000	0.45−0.80	$\mathcal{O}(0.10)$
	1002−1003	1002−1003	1000	0.90−1.25	$\mathcal{O}(0.18)$
0.30	1022 ± 0.5	1017 ± 0.5	1000	0.21	$\mathcal{O}(0.01)$
	1016 ± 0.5	1012 ± 0.5	1000	0.30	$\mathcal{O}(0.02)$
	1009 ± 0.3	1007 ± 0.3	1000	0.47	$\mathcal{O}(0.04)$
	1006 ± 0.3	1005 ± 0.3	1000	0.63	$\mathcal{O}(0.06)$
	1005 ± 0.2	1004 ± 0.2	1000	0.75	$\mathcal{O}(0.08)$

For $S = 0.3$, the notation $\rho = A \pm B$ represents A as a nominal value with B as the variation in A across different experiment to maintain nearly constant values of S. δD_m is the corresponding uncertainty in measured D_m. All densities are measured in kg/m^3

The air curtain was installed on the saltwater side next to the lock gate, as shown in Fig. 2. It was fabricated from a cylindrical pipe of length 182 mm, which was closed at its ends. A fine sponge wrapped in a flexible steel wire mesh was fitted inside this cylinder to facilitate a uniform distribution of the air curtain fluid. 32 pinholes of size $\phi_p = 1.1$ mm, as shown in the top left side of Fig. 2, were uniformly drilled using a vertical milling machine along the length of the cylinder. In any experiment, the air curtain was installed such that these holes were just submerged in saltwater. The resultant round water jets from these holes usually merge a few diameters downstream of the cylindrical pipe and form a planar jet required for the sealing [39]. The effective planar jet width can be estimated as the ratio of the total area over which the flow occurs to the cylinder length and is equal to 0.17 mm in the present experiments.

The fluid supply for the ACD is taken from a tank (denoted as ST) using a centrifugal pump whose delivery head is regulated through a control valve, V1. In the case of NBAC, salt is dissolved in the supply tank such that $\rho_0 = \rho_d$ and $\Gamma_0 = \Gamma_d$ where Γ denotes the electrical conductivity of the solution. Whereas for HAC, we dissolve excess sugar in the curtain fluid such that $\rho_0 > \rho_d$ for establishing the extra buoyancy. However, the conductivity, in this case, is related as $\Gamma_0 < \Gamma_d$. The reason behind using sugar instead of salt for creating a heavy air curtain will be discussed later. The flow rate through the air curtain nozzle is measured using a turbine flowmeter (TFM) with an accuracy of $\pm$ 3%. Another control valve, V2, was provided to fine-tune the flow rate to a predetermined value which was kept constant at $Q_0 = 6$ LPM across all the experiments (see Table 3).

After filling the tank to the desired level, fluids on the two sides are stirred to ensure a homogeneous medium. Six samples are then collected from each half of the tank at different spatial locations. The density and conductivity of these samples are measured using the Anton Paar DMA 1001 density meter (accuracy: $\pm$ 0.0001 gm/cc) and Thermo Scientific A222 conductivity meter (accuracy: $\pm$ 0.5%). The random error in these measurements is within $\pm$ 0.0002 gm/cc and $\pm$ 0.5%, respectively. The estimates of the salt concentration, c (in gm/L), are derived from the measured conductivity through

a calibration that was performed for a known amount of salt concentrations ranging between 0 to 80 gm/L. The air curtain is then switched on, and the flow is allowed an establishment time (usually of the order of $t_0 = 10$ s), after which the flow rate through the ACD becomes nearly constant. The initial difference of 5 mm in the fluid levels is provided for this adjustment such that at the time of removing the lock-gate, the free surfaces on both sides are at the same level. Upon the establishment of the air curtain, the lock gate is rapidly removed for the commencement of the fluid exchange. The ACD continues to operate for $t_{ex} = 45$ s, during which a high speed camera, described below, records the entire exchange process. The lock gate is then reinstalled firmly, followed by switching off the air curtain and closing of valve V2 to avoid any possible return flow that may occur due to gravity-induced siphon. Subsequently, the fluid in each half of the tank undergoes the homogenization process as described above. At the end of the experiment, samples are taken from the indoor region to measure ρ_d^n and Γ_d^n that provides an estimate of the exchange that occurred during the time span of t_{ex} seconds, where the superscript n represents the new values of the corresponding property.

To visualize the bulk structure of air curtains, a colored dye (laundry brightener) was injected through a 0.8 mm needle placed near the jet exit. The dye injection was gravity driven from a small supply tank (shown as DIT), and its flow rate was regulated using a control valve, V3. The needle head was carefully positioned, and the valve was adjusted such that a dye parcel loses its momentum completely after reaching underneath the air curtain. In most experiments, the dye injection starts at $t = t_0$ after removal of the lock-gate and finishes at $t = t_0 + t_{ex}$ just before the LG is reinstalled. In some experiments, another dye was premixed with the outdoor fluid (freshwater) to observe the infiltration that occurs during a door opening cycle. The resultant flow is imaged using a Canon EOS 90D DSLR camera with an adjustable focal length (18–135 mm) lens at a sampling rate of 100 Hz.

To quantify the amount of fluid exchange during the air curtain operation, we employ the mass conservation in the indoor space, similar to that adopted by Frank and Linden [18], Jha et al. [20], which yields:

$$\rho_d^n(V + V_{ACD}) = \rho_d V - \rho_d V_{ex} + \rho_l V_{ex} + \rho_0 V_{ACD} \tag{17}$$

Here, the left-hand side represents the total mass in the dense (indoor) fluid region at the end of an experiment. The initial volume, V, of the indoor space is taken as $\frac{LWH}{2}$ and V_{ACD} accounts for the volume of the air curtain fluid added to the indoor space and is calculated as $V_{ACD} = 0.5Q_0t_0 + \beta Q_0 t_{ex}$. In this expression, $0.5Q_0t_0$ approximates the volume of fluid added to the indoor space during the start-up phase assuming a linear variation of flow rate (in time) from 0 to Q_0. In the second term, β accounts for the spillage of the air curtain inside the dense fluid half after impingement on the floor of the tank and is taken as 0.5 in the subsequent calculations. This value of β was also chosen in the experimental studies conducted by other researchers [11, 17, 18]. In addition, our numerical simulations also confirm that the air curtain jet divides nearly equally between the two halves after impingement. The first term on the right-hand side of Eq. (17) is the initial mass of the region under consideration, whereas the second and third terms represents the mass transfer across the doorway owing to fluid exchange. The corresponding volume exchange is represented as V_{ex}. The last term signifies the mass added due to the air curtain operation. For a neutrally buoyant air curtain, $\rho_0 = \rho_d$, and the corresponding exchange flow rate across the air curtain device, q_{ACD}, can be estimate as:

$$q_{ACD} = \frac{V_{ex}}{t_{ex}} = \left(\frac{\rho_d - \rho_d^n}{\rho_d - \rho_l}\right)\left(\frac{V + V_{ACD}}{t_{ex}}\right) \tag{18}$$

For a heavy air curtain, since $\rho_0 > \rho_d$, the final density in the indoor space, ρ_d^n, can change either due to infiltration of the ambient fluid of density ρ_l or due to the addition of the air curtain of density ρ_0. It should be noted that while the infiltration from the ambient space results in a reduction of the mean fluid density within the indoor region, the air curtain device, owing to the added buoyancy, increases the mean density. To quantify the overall fluid exchange, a mass conservation equation similar to Eq. (17) can still be formulated for a HAC, however, it cannot explicitly differentiate between the two aforementioned contributions and, therefore, only provides an *apparent* estimate of the exchange flow based on the mean density, ρ_d^n, within the indoor space. Consider a scenario where a contaminant is present in the ambient fluid, and some exchange takes place between the indoor and outdoor space. It is possible that the reduction in the fluid density in the indoor space due to this exchange may be counterbalanced by the air curtain device and thus, the effectiveness based on Eqs. (2 and 18) may not reflect the sealing capabilities of an ACD associated with the transport of such contaminants. Therefore, one needs to segregate the infiltration effect of the ambient fluid from the air curtain contribution to ρ_d^n. This can be achieved by introducing a different tracer (sugar) for the air curtain device which distinguishes between the ambient and the ACD fluids. A conservation equation for the "salt mass", as was first proposed by Frank and Linden [18], can now be written for the dense fluid half as:

$$c_d^n(V + V_{ACD}) = c_d V - c_d V_{ex} + c_l V_{ex} + c_0 V_{ACD} \tag{19}$$

The physical meaning of individual terms in Eq. (19) is identical to that of Eq. (18), where the total mass is replaced using the salt mass, which can be inferred from the measured salt concentration c. An algebraic rearrangement of Eq. (19) leads to:

$$q'_{ACD} = \frac{V_{ex}}{t_{ex}} = \left(\frac{c_d - c_d^n}{c_d - c_l}\right)\frac{V}{t_{ex}} + \left(\frac{c_0 - c_d^n}{c_d - c_l}\right)\frac{V_{ACD}}{t_{ex}} \tag{20}$$

For a neutrally buoyant air curtain, $c_0 = c_d$ and $\rho_0 = \rho_d$, and thus Eqs. (18 and 20) are identical. Whereas for a heavy air curtain, $c_0 = c_l < c_d$ and $\rho_0 > \rho_d > \rho_l$, therefore, the exchange flow rate associated with the salt mass transfer in Eq. (20) may be different than that of Eq. (18). In the context of building flows, measuring the density ρ_d^n and the associated q_{ACD} could be a possible surrogate for the mean fluid temperature within the indoor region and thus, can be a good indicator of thermal comfort for building occupants. On the other hand, the corresponding measurements of q'_{ACD} could act as a proxy for fluid infiltration from the ambient space. For the same reasons, the effectiveness based on the measure of exchange flow in Eq. (20) may be different from E (Eq. 2) and can be calculated as $E' = 1 - \frac{q'_{ACD}}{q'}$. Both of these measures are reported in Sect. 5.2.

4 Analytical description

In this section, we present an analytical model to describe the spatial evolution of an air curtain jet. A domain similar to that of our simulations, with two fluids at densities, ρ_d and ρ_l, is considered, as shown in Fig. 3a. An ACD with an initial density, ρ_0, and a uniform velocity, w_0, is provided at the interface between the two fluids. The small density

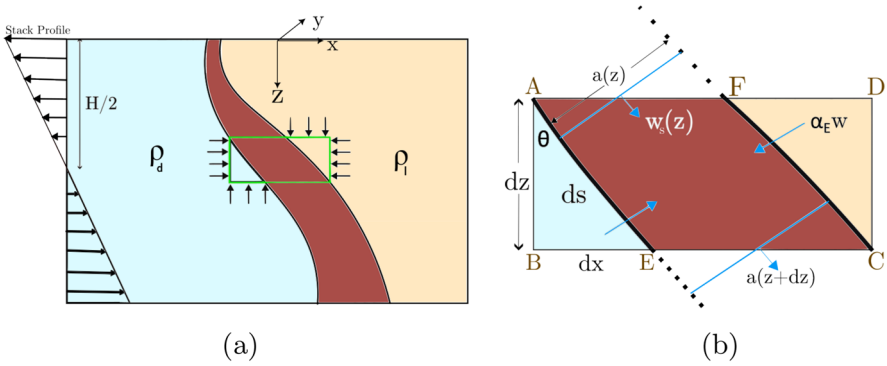

Fig. 3 Control volume chosen for the formulation of the analytical model

differences in the system imply that the Boussinesq approximation is applicable. We also consider that the jet width at the nozzle exit, a_0, is much smaller compared to the span of the domain, thereby enabling a two-dimensional formulation of the analytical model, which is valid for present experiments. In addition, the jet is considered to be uniform along the spanwise (y) direction, so that the dynamical quantities could be evaluated per unit length of the plane buoyant jet.

Consider a rectangular control volume $ABCD$ as shown in Fig. 3b, where the air curtain is having an arbitrary geometric configuration defined by the width, $a(z)$, and an inclination angle $\theta(z)$. The analytical model, outlined next, is based on the Newtonian conservation equations applied to this Eulerian control volume. The framework presented below for the analytical development is similar to that of Frank and Linden [18], however in the present work, the sense of buoyancy flux is reversed owing to different practical motivation. In addition, we have also utilised the developed model for studying the vertical evolution of mean velocity of the air curtain and its deflection as discussed later.

First, we write the equation for the conservation of volume flux. Physically, it implies that the total fluid volume leaving the face EC, $Q(z+dz)$, must equal to that entering through AF, $Q(z)$ and the volume being entrained through faces AE and FC, Q_E. To quantify the fluid entrainment, we use the model proposed by Morton, Taylor and Turner [40], according to which the entrainment velocity u_E is taken to be proportional to a characteristic velocity scale of the flow with the proportionality constant being the entrainment coefficient α_E. For the case of jets, this characteristic velocity is usually taken to be the centerline velocity, $w_s(z)$. It is to be noted that the fluid entrainment, owing to the tilt of the air curtain, takes place along the interfaces AE and FC, which may not necessarily be vertical. Therefore, to accommodate for the slant angle θ, we consider the flux along $ds = dz\sqrt{1+\tan^2\theta}$. The resultant volume conservation equation therefore becomes:

$$\frac{d}{dz}(aw_s) = \alpha_E w_s \sqrt{1+\tan^2\theta} \tag{21}$$

The next set of conservation equations are derived from the two components of the total momentum flux, $m = aw_s^2$. We first consider the horizontal component of the total momentum flux, $m_x = aw_s^2 sin\theta$, where the only force affecting the fluid momentum is due to the ambient stack effect resulting from the horizontal density stratification. For an isothermal

jet, this force will be zero. In the context of building flows, it should be highlighted that this forcing is zero at the *neutral height* where the outside and inside fluid pressures are same. A representative stack profile is also shown in Fig. 3a. It has previously been shown that the location of neutral height has a significant effect on the dynamics of fluid exchange that occurs in buildings [17]. The horizontal momentum flux equation, therefore, under the Boussinesq approximation, can be written as:

$$\frac{d}{dz}\left(aw_s^2 \sin\theta\right) = -g'\left(z - \frac{H}{2}\right) \tag{22}$$

where z is measured from the nozzle exit. On the other hand, in the vertical direction, the corresponding momentum flux $m_z = aw_s^2 cos\theta$ could change due to two effects. First, a net pressure difference that acts between the faces *BE* and *FD* of the control volume. Here, the length element dx can be expressed as $dz\ tan\theta$ to estimate the component of this pressure force acting in the vertical direction. The second contribution to the vertical momentum is owing to the buoyancy force, $g(\rho - \rho_d)$, that the air curtain experiences as it penetrates in the ambient fluid. Therefore, the resulting equation for the momentum flux conservation in z-direction assumes the following form:

$$\frac{d}{dz}\left(aw_s^2 \cos\theta\right) = g'\left(z - \frac{H}{2}\right)\tan\theta - \frac{ag}{\cos\theta}\left(\frac{\rho}{\rho_d} - 1\right) \tag{23}$$

Lastly, considering the initial density difference at the nozzle exit, $\rho - \rho_d$, and invoking the conservation of the associated buoyancy flux per unit jet length, $aw_s b$, yields:

$$\frac{d}{dz}\left(aw_s g\left(\frac{\rho}{\rho_d} - 1\right)\right) = 0 \tag{24}$$

To simplify the equation set (21)–(24), we note that the characteristic velocity and length scales, w_s and a, can be expressed as m/Q and Q^2/m respectively where $m = \sqrt{m_x^2 + m_z^2}$ with $tan\theta = m_x/m_z$. This yields the following equations which are subsequently solved in MATLAB to obtain the spatial evolution of the air curtain jet:

$$\begin{aligned}
&\frac{d}{dz}(Q) = \frac{\alpha_E}{m_z}\frac{m_x^2 + m_z^2}{Q}\\
&\frac{d}{dz}\left(m_x\right) = -g'\left(z - \frac{H}{2}\right)\\
&\frac{d}{dz}\left(m_z\right) = +g'\left(z - \frac{H}{2}\right)\frac{m_x}{m_z} - \frac{Q^2 b}{m_z}\\
&\frac{d}{dz}(Qb) = 0
\end{aligned} \tag{25}$$

For a vertically blowing ACD installation with an exit velocity w_0 and density ρ_0, the initial conditions for the variables describing equation set 25 are:

$$
\begin{aligned}
Q(0) &= Q_0/W \\
m_x(0) &= 0 \\
m_z(0) &= a_0 w_0^2 \\
b(0) &= g\left(\rho_0/\rho_d - 1\right)
\end{aligned}
\tag{26}
$$

5 Results

In this section, we would first present a qualitative description of the buoyancy (temperature) field in the domain obtained from the experiments and simulations. This allows demarcation of an ACD installation into an unstable or a stable regime. Subsequently, we calculate the performance of neutrally buoyant and heavy air curtains in the form of sealing effectiveness using different methodologies and discuss the implications of an assisting buoyancy towards better climatic separation. In the last part of this section, a quantitative analysis comparing the velocity statistics of an air curtain jet with an isothermal jet is presented.

5.1 Structure of the air curtain flow

Figure 4 presents a comparison of the dye visualization obtained from the experiments with that of the buoyancy distribution predicted by the LES simulations. In experiments, a green

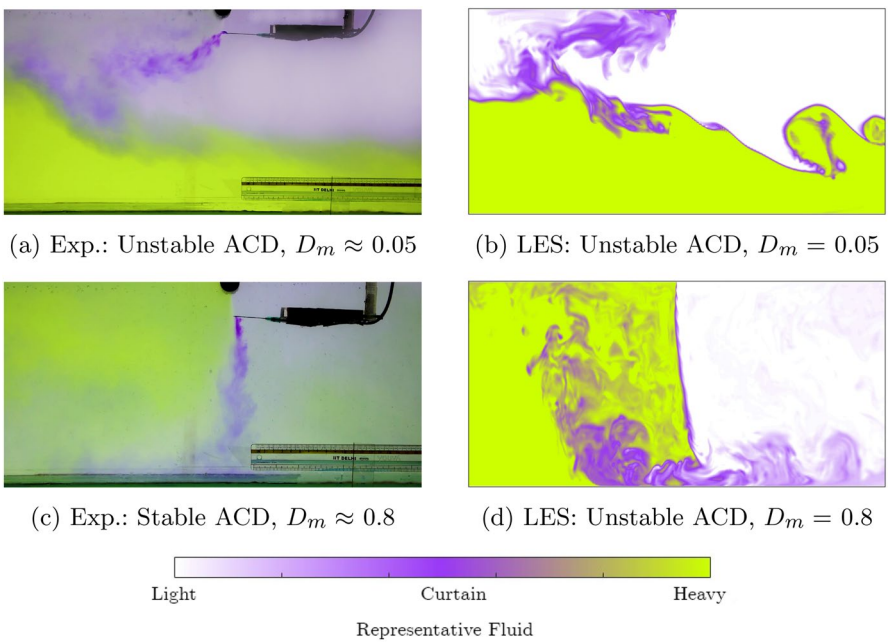

Fig. 4 Comparison between the experimental flow visualization and the pseudocolor buoyancy contours of the LES simulations at different deflection modulus

dye was premixed with the dense fluid, whereas the laundry brightener (blue) was used to mark the curtain fluid of density ρ_0. The resultant flow field for two values of deflection modulus, D_m, is shown in Fig. 4a and c respectively. At small values of D_m, the ACD fails to reach the opposite end of the doorway and is deflected sideways due to the disruptive buoyancy difference across it. As a result, there is infiltration of the ambient fluid (notice the trajectory of the air curtain) accompanied by leakage from the indoor region. This regime is, therefore, commonly referred to as an unstable (or breakthrough). The buoyancy distribution obtained from the LES simulation of an unstable ACD is shown in Fig. 4b. Here, it should be pointed out that while the blue color corresponds to an equivalent density of $\frac{\rho_d+\rho_l}{2}$, it is a reasonably good marker for the air curtain fluid that separates the indoor and outer regions. From simulations, the data is extracted from the center plane ($y = L_y/2$) to illustrate the characteristic features associated with the air curtain flows. The presence of overturning vortices at the interface between the light (white) and the dense (green) fluid is attributed to shear instability. Note that these features are not evident in experimental images since the camera sensor inevitably performs a spatial averaging across the width/span of the tank during the recording process. Overall, a good qualitative agreement can be observed between experiments and simulations.

When the momentum flux of the air curtain is increased while keeping the stack effect the same, i.e., as D_m increases, the jet possesses sufficient strength to reach the other end. As a result, a near-vertical trajectory is established, which is also predicted by the numerical computations as shown in Fig. 4d. This results in an aerodynamic barrier that significantly suppresses the pure buoyancy-induced exchange that occurs at small D_m. However, as the jet travels from the nozzle exit to the bottom wall, some amount of fluid is entrained into the jet leading to a slight dilution. In addition to this, upon impingement of the ACD on the floor, the jet is divided into two parts that travel to the indoor and outdoor spaces. While the flow physics of this impingement region is not properly understood, it is likely that the high turbulence in this region results in some fluid exchange across the air curtain, leading to an effectiveness smaller than unity.

5.2 Air curtain effectiveness

In this section, we first quantify the sealing effectiveness corresponding to the neutrally buoyant air curtains and validate our results with the existing literature. Subsequently, we present estimates of E for heavy air curtains and compare them with their neutral counterparts to assess the influence of the assisting buoyancy.

5.2.1 Neutrally buoyant ACDs

A neutrally buoyant air curtain comprises a jet having the same density as that of the space it is discharging into, i.e., $\rho_0 = \rho_d$. The effectiveness can be calculated using the primitive definition introduced in Eq. (2) which compares the fluid exchange in the presence of an ACD with the case when the doorway is unprotected. Herein, the exchange flow rates are estimated using Eq. (18), which takes into account the density of the indoor fluid at any time instant t. It is to be noted that the effectiveness would also vary with time, and in this paper, we present the values of ACD effectiveness at a quasi-steady state when the exchange flow rates are nearly constant. The variation of the estimated effectiveness as a function of deflection modulus is shown in Fig. 5 for all the methodologies and are compared with the experimental values of [20] who conducted measurements in a facility of

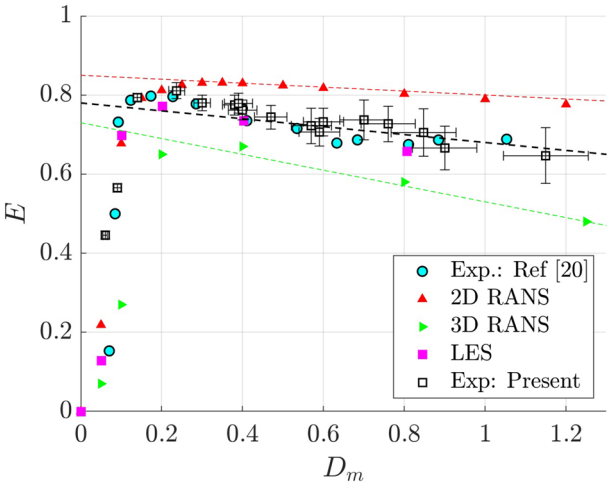

Fig. 5 E vs. D_m curve obtained from the experiments and compared with the measurements of Jha et al. [20] and the LES data

similar size with similar operating conditions in the same range of D_m. An open door situation corresponds to $D_m = 0$.

Firstly, the qualitative variation is represented accurately using both numerical and experimental techniques. The sealing effectiveness assumes low values for unstable ACDs ($D_m \lessapprox \mathcal{O}(0.1)$ for which the air curtain breakthrough and allows a certain amount of fluid exchange to occur. As the deflection modulus is increased, the values of E correspond to a typical stable configuration for which the E_{max} are approximate of the order 0.8, i.e., only 20% of the original exchange flow remains across the air curtain. Upon an increment in the D_m beyond this point, a gradual reduction in the sealing effectiveness is observed, which is likely due to stronger turbulence in the impingement region that results in mass transfer.

Second, it can be seen that the effectiveness predicted by the RANS-based numerical simulations differs considerably from the experimental measurements. Generally, we observe that for 2D computations, the values of E are over-predicted beyond a D_m of 0.2, whereas the 3D framework results in an under-prediction. A trend line for the stable ACDs is also shown in Fig. 5 that shows the difference in magnitude from the experimental measurements, which is denoted using the black dashed line. Upon careful observation of the buoyancy distribution in various simulations, it is seen that the two-dimensional computations fail to accurately reproduce the physical phenomenons of vortex stretching, due to which the overturning motions do not cascade into smaller scales. Therefore, the unavailability of a third direction leads to an overall lower fluid exchange in the presence of an air curtain resulting in a higher effectiveness. Whereas in the corresponding LES data, we observe a very good collapse with the experimental estimates, i.e., within the experimental uncertainty limits ($\approx 5\%$). This is not surprising since the LES explicitly calculates the motion of large eddies, which are largely responsible for the bulk exchange associated with air curtain flows. The effect of the modeled (subgrid) scales, as it appears, does not significantly affect the estimated value of q.

Finally, as evident from Fig. 5, the present experiments also conform very well to that of the measurements of Jha et al. [20] and the LES data. This also serves as a validation for the data acquisition and analysis techniques for our measurements. Using the same process, we then alter the operating density of the air curtain to create a HAC such that $\rho_0 > \rho_d$ and the corresponding effectiveness estimates are discussed next.

5.2.2 Influence of assistive buoyancy

It is expected that the added buoyancy ($B_a \propto (\rho_d - \rho_0)$) would suppress the effects caused due to the infiltrating exchange flow ($B_i \propto (\rho_d - \rho_l)$). Overall, the indoor fluid density $\rho_d^n(t)$, at the end of an experiment (or simulation), would be a manifestation of the competing effect of B_a and B_i. Therefore, any assisting buoyancy, i.e., $S > 0$, is likely to result in higher effectiveness than its neutral counterpart ($S = 0$).

The parametric variation between E and S was studied using the 2D RANS simulations due to their lower computational cost and is shown in Fig. 6a. It can be seen that the effectiveness increases as the positive buoyancy (S) increases, irrespective of the value of D_m. The change in the sealing effectiveness relative to a neutrally buoyant air curtain, $\frac{\Delta E}{E_{NBAC}}$, was observed to be around 10 - 20% for $S = 0.3$, which is also investigated using LES and experiments and is discussed later. It is also possible that for a large value of S ($\rho_0 \gg \rho_d$), the effectiveness could exceed unity, implying that the temperature within the indoor space would be lower than $T_d = 25$ °C at the end of the simulation. However, in the present computations, the maximum value of S was taken to be 0.39, which did not exhibit this behavior for $D_m \leq 1.5$. As established in the last section, 2D RANS simulations often over-predict the values of E associated with air curtain flows, and the same is observed for the case of HAC, as discussed next.

The estimates of the sealing effectiveness obtained using the experiments, and that of the LES computations are plotted in Fig. 6b. Through both methodologies, a positive correlation is observed between E and S; however, a minimal increment (of $\mathcal{O}(5\%)$) is observed in the heavy air curtains as compared to their neutral counterpart. Equivalently, it implies that the fluid infiltration associated with a HAC installation is 25% lesser as compared to a neutrally buoyant ACD. Frank and Linden [18] computed the effectiveness of buoyant air curtains (with equivalent $\rho_0 < \rho_d$) thus making them negatively buoyant. They showed experimentally that the effectiveness, E, reduces with increasing the extent of opposing buoyancy i.e. a lighter air curtain is less effective. The findings of the present study are, therefore, in line with the previous work.

In addition, the usage of two scalars (salt and sugar) in the experiments allowed an estimation of the exchange flow based on the infiltration effect as discussed in Sect. 3 using Eq. (20). While the conventional definition, E, provides a quantitative measure

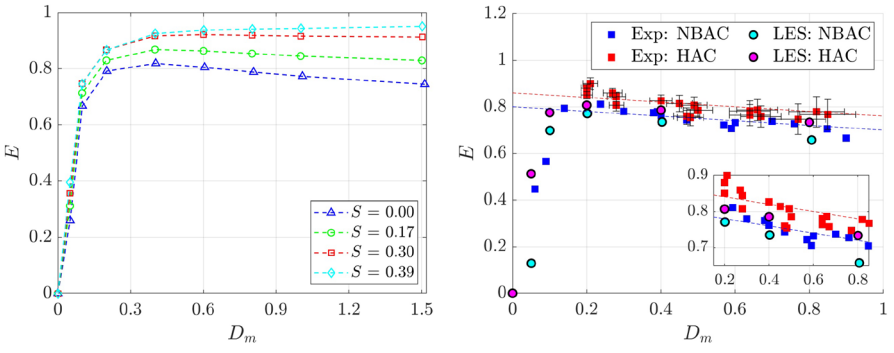

(a) 2D RANS for varying S. (b) Experiments and LES for $S = 0.3$.

Fig. 6 Estimates of the sealing effectiveness of heavy air curtain from various methods

accounting for the thermal comfort of building occupants in this context, the alternate definition based on the infiltration, E', focuses on the effect of contamination transport, therefore, providing a metric for indoor air quality. Our measurements suggest a difference of less than 2% in the calculated values of E and E', thereby indicating a good coupling between the effect of an added buoyancy on the thermal comfort as well as the indoor air quality of building space. A similar procedure could be adopted in the numerical simulations to differentiate between the two measures of effectiveness by introducing passive scalars, which could be a potential problem for future research.

5.3 Velocity statistics

The buoyancy difference across an air curtain is a significant contributor towards influencing the flow dynamics when compared to an isothermal jet. The case of an isothermal jet is a widely studied problem [5, 23, 41] and, therefore, will now be used to compare the velocity statistics at varying deflection modulus for the HAC case with $S = 0.3$. At this junction, it shall be reiterated that an ACD with smaller D_m corresponds to a higher buoyancy difference across it, whereas an ACD approaches an isothermal jet as $D_m \rightarrow \infty$.

The instantaneous velocity fields are first spatially averaged in the spanwise direction within $y = 0.04$ m $(0.25W)$ and $y = 0.13$ m $(0.75W)$ to exclude the wall effects that are present at $y = 0$ and $y = W$. Then, a temporal averaging operator is applied during the time period when the exchange flow rate exhibits a quasi-steady behavior. It should be mentioned at this point that a steady-state solution for the present ACD configuration is not possible, as the density difference across the air curtain would asymptotically approach a value of zero. Mathematically, this averaging can be written as:

$$\overline{w}(x,z) = \frac{\int_{T_1}^{T_2}\int_{Y_1}^{Y_2} w(x,y,z,t)\,dy\,dt}{(T_2 - T_1)(Y_2 - Y_1)}$$

To estimate the velocity statistics along the ACD centerline, we identify the location of the centerline, $x_{CL}(z)$, based on the maxima in vertical velocity component at any horizontal cross-section, $\overline{w}(x)$. To include the possibility that this velocity maxima could occur between two grid points, we fit a second-order polynomial around the centerline location $(x_{CL}(z))$. This process is repeated for all the grid points in the z direction to obtain $\overline{w}_{CL}(z)$. In a similar manner, the corresponding RMS velocity field is obtained along the ACD centerline as:

$$\overline{w'}(x,z) = \sqrt{\frac{\int_{t=T_1}^{t=T_2}\int_{y=Y_1}^{y=Y_2}[w(x,y,z,t) - \overline{w}(x,z)]^2\,dy\,dt}{(T_2 - T_1)(Y_2 - Y_1)}}$$

These statistics are then normalised using the exit velocity, w_0, which is a common practice for jet studies, and are shown in Fig. 7.

It can be observed from Fig. 7a that the mean centerline velocity for the isothermal jet obtained using the present simulations agrees very well with the analytical solution [42] in the self-similar region which spans roughly between $z = 0.2H$ and $z = 0.8H$. With the introduction of a buoyancy difference across the jet, $\overline{w}_{CL}(z)$ was found to be lower than its isothermal value in the self-similar region. This reduction was observed to be larger as D_m decreases and, therefore, can be attributed to the transverse stack effect, which was shown to deflect the ACD sideways providing it with a horizontal momentum. In fact, for the unstable ACD at $D_m = 0.05$, the decay rate of the centerline velocity, $\frac{d\overline{w}_{CL}}{dz}$, near the jet exit, was found to be

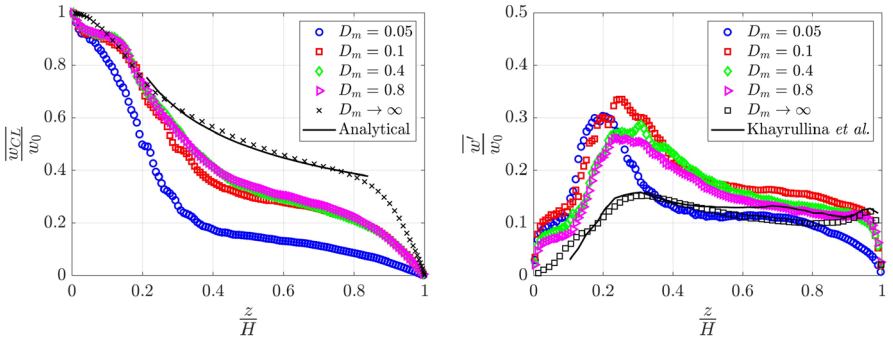

(a) Normalized centreline velocity (b) Normalized RMS velocity

Fig. 7 Comparison of the mean centerline and RMS vertical velocity obtained from the LES simulation at different D_m to quantify the differences between an air curtain and an isothermal jet

maximum, likely due to a complete sideward deflection. Whereas for the stable air curtain installation, while the decay rate was larger as compared to an isothermal jet, it was observed to be less sensitive to D_m as shown in Fig. 7a. Our preliminary analysis suggests that the entrainment of ambient fluid is larger at smaller values of D_m, which provides a pathway for the ACD deceleration along the centerline. It can also be noted that the $D_m = 0.1$ case matches quite well with that of higher D_m cases suggesting the possibility that the stability of the heavier air curtain is established at a value slightly lower than the theoretical estimate of $D_{m,min} = \frac{1}{8}$ for the neutrally buoyant air curtain. This is due to the added buoyancy provided in the ACD which allow a deeper penetration of the curtain fluid into its ambient.

On the other hand, Fig. 7b depicts an interesting behavior for the RMS vertical velocity. Similar to the isothermal jet, two peaks are obtained in the distribution of $\overline{w'}$ at $z \approx 0.3H$ and $z \approx 0.95H$. Physically, the first peak corresponds to the location of maximum turbulence intensity after the initial development of the planar jet, where the individual shear layers across the jet merge. In contrast, the second peak is due to the presence of the impingement region, where the local turbulence intensity is observed to be larger. Overall, there is a good agreement between these numerical results with the measured estimates of Khayrullina et al. [4]. It is found that the magnitude of the second peak associated with the air curtains matches very well with that of an isothermal jet, suggesting that the fluctuating field behaves very similar near the wall, and the buoyancy has negligible effects. In comparison, the normalized RMS value corresponding to the first peak for ACDs is higher than an isothermal jet and does not exhibit any significant D_m dependence either.

5.3.1 Comments on the analytical model

The system of differential Eq. (25) presented in Sect. 4 are solved numerically using MATLAB. We use the explicit Runge–Kutta method to obtain the spatial evolution of the air curtain jet, having the initial conditions outlined in Eq. (26). In the following, we compare the predictions of the analytical model with the LES data.

Figure 8a and b show the variation of the centerline velocity and the curtain deflection for the case of $D_m = 0.4$. To obtain the path traversed by the ACD in the vertical direction, we first calculate θ as $tan^{-1}\left(\frac{m_x}{m_z}\right)$ and use the expression $dx = dz\ tan(\theta)$ to quantify $x(z)$.

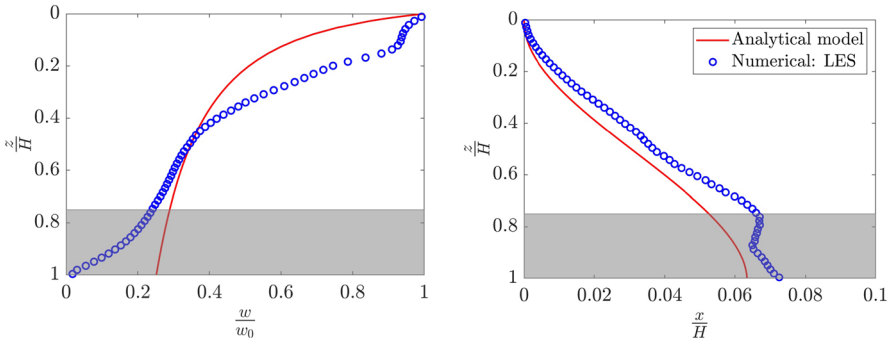

(a) Comparison of vertical velocity (b) Air curtain deflection

Fig. 8 Comparison between the predictions of the analytical model and that of simulation (LES) data corresponding to a stable air curtain at $D_m = 0.4$

The comparison of the air curtain deflection between the analytical model and the LES data seems reasonably good. The jet exhibits a minor deflection towards the outdoor space due to horizontal buoyancy $g(\rho_d - \rho_l)$. Beyond $z/H \approx 0.75$, the plane impinging jets behave differently than a free jet [4], and this region is shaded in Fig. 8. In contrast, significant discrepancies exist in the centerline velocity predicted by the analytical model. Most notably, this formulation does not account for the no-penetration boundary condition that should be imposed at $z = H$. The initial decay rate also seems to be overestimated by the model. Therefore, it can be formally concluded that while the analytical formulation predicts the trajectory of an air curtain reasonably well, it may not provide good estimates of the dynamical quantities associated with it.

6 Conclusions

Numerical simulations and experiments were conducted to quantify the sealing effectiveness, E, of neutrally buoyant and heavy air curtains. This measure of E determines the level of thermal comfort within a building which could be affected by the infiltration of outdoor fluid through any opening in the building fabric. 2D RANS, 3D RANS and LES computations were performed to understand the influence of deflection modulus, $D_m = \frac{\rho_0 a_0 w_0^2}{gH^2\Delta\rho}$, and the density ratio, $S = \frac{\rho_0 - \rho_d}{\rho_d - \rho_l}$ on the resultant exchange flow. On the other hand, dye visualization and bulk density/conductivity measurements were facilitated to provide experimental measure of the general structure of air curtain flows and their corresponding sealing effectiveness.

We compared the effectiveness of neutrally buoyant air curtains (NBAC) obtained from the LES simulations with the literature data and found a satisfactory agreement. Whereas some discrepancies were observed when the RANS solver was employed, likely due to inherent modeling of various flow scales. In addition, a good match of sealing effectiveness was also observed with the present experiments. Upon the introduction of an assisting buoyancy, it was seen that the sealing capabilities increased irrespective of the methodology adopted. This implies that the heavy air curtains positively impact the thermal comfort of building occupants at all values of D_m. As compared to the case of neutrally buoyant

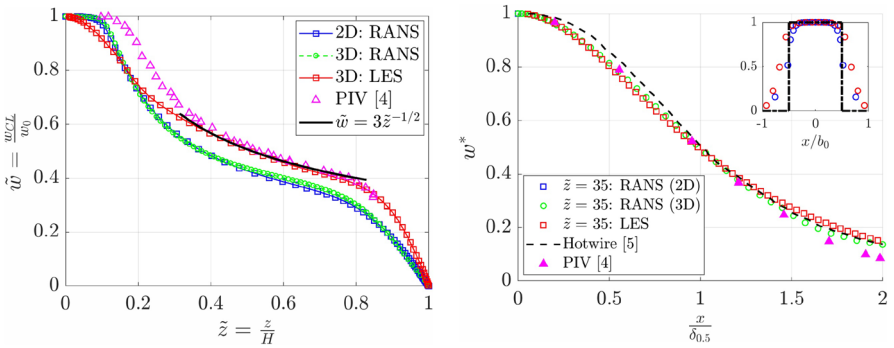

(a) Mean centerline velocity. (b) Mean velocity at $\frac{z}{a_0} = 40$.

Fig. 9 Validation of the numerical results for a plane jet at $Re = 5000$

ACDs, an increase of approximately 15% and 5% in E was estimated using 2D RANS and LES simulations for stable air curtains ($D_m \geq \mathcal{O}(0.1)$). The experimental data for the HAC also conformed with the LES estimates, which confirmed the bias associated with 2D RANS computations. Therefore, the infiltration associated with the NBACs could be suppressed by another 25% with the introduction of an assistive buoyancy.

The velocity statistics of heavy air curtains at different values of D_m were also compared to that of an isothermal jet to study the underlying effects of the various density gradients prominent in such flows. The resulting mean centerline velocity exhibited significant decay as a result of buoyancy difference across the jet. It was found that this decay was much larger for unstable air curtains where the ACD would fail to impinge on the floor and was deflected sideways. Whereas, the onset of stability in the heavier ACDs was observed near $D_m \approx 0.1$, which is smaller than NBAC measured in experiments and theoretical values.

Appendix A Numerical validation

Towards the validation of the employed numerical solvers, the case of a plane turbulent jet was simulated at a Reynolds number of 5000 and compared with the existing literature. In Fig. 9a, we compare the normalized mean vertical velocity, $\tilde{w} = \frac{\overline{w}_{CL}}{w_0}$, along the jet centerline with the analytical solution [42] and the experimental data of Khayrullina et al. [4]. A very good agreement can be observed in the self-similar region for the LES computations whereas the decay rate, $d\tilde{w}/dz$, is predicted well using both RANS and LES. This indicates the suitability of the adopted meshes and the numerical methods.

Whereas in Fig. 9b, we validate the normalized velocity profile in the self-similar region, $w^* = \frac{\overline{w}}{\overline{w}_{CL}}$, in the transverse direction x. The hotwire data of Gutmark and Wygnanski [5] is also included for this comparison. The Gaussian velocity distribution, which is characteristic of that of planar jets, is exhibited by all the numerical simulations. In the inset of this figure, the velocity distribution near the nozzle exit is plotted to illustrate the near top-hat profile supplied as the boundary condition. A detailed discussion on this validation is presented in [29].

Acknowledgements We sincerely thank the technical staff of the fluid mechanics laboratory and Mr. Ayank Raj for their invaluable assistance during the experiments. The insightful discussions with Dr. Ed Santilli from Thomas Jefferson University on setting up the LES simulations using SOMAR are highly appreciated and greatly enhanced the quality of our research. We also appreciate the constructive feedback of anonymous reviewers and Prof. Sridhar Balasubramanian for his editorial handling of the manuscript.

Author contributions Experiments were conducted jointly by TA and SA under the mentorship of NKJ. The numerical simulations and the corresponding data analysis was done by TA under the supervision of VKC. The first draft of the manuscript was written by TA and SA and all authors commented on previous versions of the manuscript. All authors read and approved the final manuscript.

Funding Tanmay Agrawal acknowledges the Prime Minister Research Fellowship (PMRF) provided by the Government of India, while Narsing Kumar Jha acknowledges the seed grant (PLN12/04AM) and matching grant (MI02572G) supports from Indian Institute of Technology Delhi.

Declarations

Conflict of interest The authors have no competing interests to declare that are relevant to the content of this article.

References

1. Jones AP (1999) Indoor air quality and health. Atmos Environ 33(28):4535–4564
2. Kaushik A, Arif M, Tumula P, Ebohon OJ (2020) Effect of thermal comfort on occupant productivity in office buildings: response surface analysis. Build Environ 180:107021
3. Hayes FC, Stoecker WF (1969) Heat transfer characteristics of the air curtain. ASHRAE Trans 2120:153–167
4. Khayrullina A, van Hooff T, Blocken B, van Heijst GJF (2017) PIV measurements of isothermal plane turbulent impinging jets at moderate Reynolds numbers. Exp Fluids 58:1–16
5. Gutmark E, Wygnanski I (1976) The planar turbulent jet. J Fluid Mech 73(3):465–495
6. Howell RH, Shibata M (1980) Optimum heat transfer through turbulent recirculated plane air curtains. ASHRAE Trans 2567:188–200
7. Gupta S, Pavageau M, Elicer-Cortes J (2007) Cellular confinement of tunnel sections between two air curtains. Build Environ 42(9):3352–3365
8. Foster AM, Swain MJ, Barrett R, D'Agaro P, Ketteringham LP, James SJ (2007) Three-dimensional effects of an air curtain used to restrict cold room infiltration. Appl Math Model 31(6):1109–1123
9. Amin M, Dabiri D, Navaz H (2011) Comprehensive study on the effects of fluid dynamics of air curtain and geometry, on infiltration rate of open refrigerated cavities. Appl Therm Eng 31(14–15):3055–3065
10. Navaz H, Henderson B, Faramarzi R, Pourmovahed A, Taugwalder F (2005) Jet entrainment rate in air curtain of open refrigerated display cases. Int J Refrig 28(2):267–275
11. Jha NK, Frank D, Linden PF (2021) Contaminant transport by human passage through an air curtain separating two sections of a corridor: Part I-uniform ambient temperature. Energy Build 236:110818
12. Shih Y, Yang A, Lu C (2011) Using air curtain to control pollutant spreading for emergency management in a cleanroom. Build Environ 46(5):1104–1114
13. Guyonnaud L, Solliec C, Dufresne de Virel M, Rey C (2000) Design of air curtains used for area confinement in tunnels. Exp Fluids 28(4):377–384
14. Yu L, Liu F, Beji T, Weng M, Merci B (2018) Experimental study of the effectiveness of air curtains of variable width and injection angle to block fire-induced smoke in a tunnel configuration. Int J Therm Sci 134:13–26
15. Lv L, Zeng L, Wu Y, Gao J, Xie W, Cao C, Zhang J (2021) The application of an air curtain range hood in reducing human exposure to cooking pollutants. Build Environ 205:108204
16. Gonçalves JC, Costa JJ, Figueiredo AR, Lopes AMG (2012) CFD modelling of aerodynamic sealing by vertical and horizontal air curtains. Energy Build 52:153–160
17. Frank D, Linden PF (2014) The effectiveness of an air curtain in the doorway of a ventilated building. J Fluid Mech 756:130–164
18. Frank D, Linden PF (2015) The effects of an opposing buoyancy force on the performance of an air curtain in the doorway of a building. Energy Build 96:20–29

19. Bacot A, Frank D, Linden PF (2022) Bubble curtains used as barriers across horizontal density stratifications. J Fluid Mech 941:1
20. Jha NK, Frank D, Darracq L, Linden PF (2021) Contaminant transport by human passage through an air curtain separating two sections of a corridor: Part II-two zones at different temperatures. Energy Build 236:110728
21. Agrawal T, Jha NK, Chalamalla VK (2021) Towards understanding air curtain flows using rans based numerical simulations. In: Proceedings of the 26^{th} National and 4^{th} International ISHMT-ASTFE Heat and Mass Transfer Conference December 17-20, 2021, IIT Madras, Chennai-600036, Tamil Nadu, India. Begel House Inc
22. Linden PF (1999) The fluid mechanics of natural ventilation. Annu Rev Fluid Mech 31(1):201–238
23. Khayrullina A, van Hooff T, Blocken B, van Heijst GJF (2019) Validation of steady RANS modelling of isothermal plane turbulent impinging jets at moderate Reynolds numbers. Eur J Mech-B/Fluids 75:228–243
24. Ruiz CA, van Hooff T, Blocken B, van Heijst GJF (2023) Influence of cross-jet temperature and pressure differences on the separation efficiency of air curtains in buildings. J Wind Eng Ind Aerodyn 233:105300
25. Wilcox DC (1998) Turbulence modeling for CFD. DCW Industries La Canada, CA
26. Pope SB (2000) Turbulent flows. Cambridge University Press, Cambridge
27. Sagaut P (2006) Large eddy simulation for incompressible flows: an introduction. Springer
28. Yakhot V, Orszag SA, Thangam S, Gatski TB, Speziale CG (1992) Development of turbulence models for shear flows by a double expansion technique. Phys Fluids A 4(7):1510–1520
29. Agrawal T, Jha NK, Chalamalla VK (2023) Numerical investigation of air curtain flows in the doorway of a building using RANS and LES. Comput Fluids, 105948
30. Santilli E, Scotti A (2015) The stratified ocean model with adaptive refinement (SOMAR). J Comput Phys 291:60–81
31. Chalamalla VK, Santilli E, Scotti A, Jalali M, Sarkar S (2017) SOMAR-LES: a framework for multiscale modeling of turbulent stratified oceanic flows. Ocean Model 120:101–119
32. Varma D, Chalamalla VK, Mathur M (2020) Spontaneous superharmonic internal wave excitation by modal interactions in uniform and nonuniform stratifications. Dyn Atmos Oceans 91:101159
33. Passaggia PY, Chalamalla VK, Hurley MW, Scotti A, Santilli E (2020) Estimating pressure and internal-wave flux from laboratory experiments in focusing internal waves. Exp Fluids 61(11):1–29
34. Agrawal T, Peddada SH, Chalamalla VK (2022) Dynamics of a buoyant gravity current propagating in a linearly stratified medium. Phys Fluids 34(7):076605
35. Bonometti T, Balachandar S (2008) Effect of Schmidt number on the structure and propagation of density currents. Theoret Comput Fluid Dyn 22(5):341–361
36. Agrawal T, Ramesh B, Zimmerman SJ, Philip J, Klewicki JC (2021) Probing the high mixing efficiency events in a lock-exchange flow through simultaneous velocity and temperature measurements. Phys Fluids 33(1):016605
37. Frank D, Jha NK, Koene FGH, Kemp REJ, Twerda A, Linden PF (2022) Air curtains: validation of results from small-scale laboratory waterbath experiments by real-scale measurements in climate chambers and numerical simulations. Energy Build 277:112538
38. Kaye NB, Flynn MR, Cook MJ, Ji Y (2010) The role of diffusion on the interface thickness in a ventilated filling box. J Fluid Mech 652:195–205
39. Knystautas R (1964) The turbulent jet from a series of holes in line. Aeronaut Q 15(1):1–28
40. Morton B, Taylor GI, Turner JS (1956) Turbulent gravitational convection from maintained and instantaneous sources. Proc Royal Soc London Ser A Math Phys Sci 234:1–23
41. Deo RC, Mi J, Nathan GJ (2008) The influence of Reynolds number on a plane jet. Phys Fluids 20(7):075108
42. Rajaratnam N (1976) Turbulent Jets. Elsevier, Amsterdam